Research Article

Pseudohexagonal Nb$_2$O$_5$ Anodes for Fast-Charging Potassium-Ion Batteries

Guanxu Chen, Jintao Chen, Siyu Zhao, Guanjie He,* and Thomas S. Miller*

Cite This: https://doi.org/10.1021/acsami.2c21490
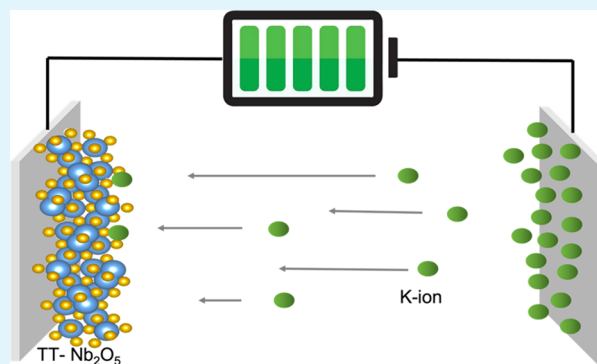
Read Online

ACCESS | ‖‖ Metrics & More | 📰 Article Recommendations | 🗊 Supporting Information

ABSTRACT: High-rate batteries will play a vital role in future energy storage systems, yet while good progress is being made in the development of high-rate lithium-ion batteries, there is less progress with post-lithium-ion chemistry. In this study, we demonstrate that pseudohexagonal Nb$_2$O$_5$(TT-Nb$_2$O$_5$) can offer a high specific capacity (179 mAh g^{-1} ~ 0.3C), good lifetime, and an excellent rate performance (72 mAh g^{-1} at ~15C) in potassium-ion batteries (KIBs), when it is composited with a highly conductive carbon framework; this is the first reported investigation of TT-Nb$_2$O$_5$ for KIBs. Specifically, multiwalled carbon nanotubes are strongly tethered to Nb$_2$O$_5$ via glucose-derived carbon (Nb$_2$O$_5$@CNT) by a one-step hydrothermal method, which results in highly conductive and porous needle-like structures. This work therefore offers a route for the scalable production of a viable KIB anode material and hence improves the feasibility of fast-charging KIBs for future applications.

KEYWORDS: KIB, potassium-ion batteries, carbon nanomaterials, PIB, niobium oxide, battery anode

1. INTRODUCTION

The growing demand for electric vehicles and portable electronic devices is driving the need for energy storage systems that overcome the numerous disadvantages associated with current technologies.[1] For example, while lithium-ion batteries (LIBs) exhibit a reasonable capacity and reliable electrochemical performance, the limited availability and uneven global distribution of lithium[2] means that their future application is at risk of over-demand or sociopolitical changes.[4] Potassium-ion batteries (KIBs) are promising alternatives as, among other factors, K has a low standard electrode potential (Li/Li$^+$: −3.04 V vs standard hydrogen electrode (SHE), K/K$^+$: −2.93 V vs SHE) contributing to a large potential window and a high energy density.[3] However, unlike lithium, potassium is relatively abundant (>2% of the earth's crust composition)[4] and much more equitably distributed around the globe, offering significant benefits in terms of resource security and sustainability.[5−7] Unfortunately, despite KIBs generally relying on similar intercalation, alloying, or conversion reactions similar to those used in LIBs, materials for K storage often suffer from low capacities, short lifetimes, or poor rate capabilities due to the significantly larger ionic radius of K$^+$ (1.38 vs 0.76 Å for Li$^+$).[8−10]

Achieving a high charge−discharge rate is a key challenge for KIBs, as K ions exhibit poor kinetics due to their large radius, and materials that have been used to try to achieve the high performance can largely be divided into two main categories: carbonaceous (e.g., hard−soft carbon composites,[11] N−S co-doped carbons,[12] phosphorus-doped carbons[13]) and non-carbonaceous (e.g., SnP$_2$O$_7$ composites,[14] potassium tetratitanate,[15] or azobenzene-4,4′-dicarboxylic acid potassium salts—ADAPTS[16]). Yet unfortunately, carbonaceous anodes can achieve good cyclability, but they exhibit relatively poor rate compatibility at scan rates higher than 1C. Regarding the pure noncarbonaceous materials, the high cost of raw materials hindered their commercialization. In addition, noncarbonaceous anodes, in general, cannot achieve good cyclability, good rate performance at scan rate over 20C, and high specific capacity at the same time.

Niobium (V) oxide (Nb$_2$O$_5$) has been widely investigated as a high-rate anode for LIBs as it offers cyclic stability, high capacity, and outstanding reversibility.[17−21] It has also gained attention as an anode for sodium-ion batteries (SIBs) in recent years, despite its somewhat modest rate performance.[22−29] However, to date, only a small number of studies have examined the electrochemical performance of Nb$_2$O$_5$ as an anode material for KIBs, despite the fact it has a large lattice spacing (3.93 Å) that can accommodate K ions.[30] Nonetheless, previous reports have shown that the orthorhombic form of

$Nb_2O_5(T-Nb_2O_5)$ can offer good capacities in KIBs at low rates and over reasonably long cycle lifetimes.[24−27] For example, Li et al.[31] investigated $T-Nb_2O_5$ nanowires as KIB anodes, which delivered a specific capacity of 127 mAh g^{-1} at 0.2 A g^{-1}, whereas Yuan et al.[32] designed a $T-Nb_2O_5$ N-doped carbon composite, which showed a capacity of 161 mAh g^{-1} at 0.1 A g^{-1}. However, they also show that $T-Nb_2O_5$ in KIBs does not perform as well at high rates as it does in LIBs. Nonetheless, other forms of Nb_2O_5 do exist, such as pseudohexagonal $Nb_2O_5(TT-Nb_2O_5)$, which offers benefits including lower-temperature synthetic conditions and a tendency toward a smaller average particle size.[33] Yet, $TT-Nb_2O_5$ has not, to date, been assessed as an anode material for KIBs.

Like many other transition metal oxides (TMOs), Nb_2O_5 is a semiconductor with a relatively wide band gap, meaning that it can be difficult to use directly as an electrode in most batteries due to its low electrical conductivity.[34,35] The two most widely applied strategies to overcome this issue are either reducing the size of the TMOs to the nanoscale or combining the TMOs with conductive materials (often carbonaceous— e.g., graphite,[18,36] graphene,[37−39] reduced graphene oxide (rGO),[40,41] or carbon nanotubes (CNTs)[42−45]). CNTs, as commercialized and cost-effective materials, offer particular advantages in electrode composites as their excellent mechanical, electrical, and thermal properties will increase electrical conductivity, enhance electrode stability, and improve the electrode structure. However, to uniformly deposit TMO nanoparticles (NPs) onto CNTs is challenging as unfunctionalized CNTs are difficult to disperse evenly in aqueous solutions and tend to form weak links with nanoparticles due to the lack of surface groups to act as sites for tethering.[41]

Herein, we assess the capability of pseudohexagonal Nb_2O_5 for use as anodes in KIBs for the first time, enabled via a designed carbon framework. Although $TT-Nb_2O_5$ is less ordered than its crystalline analogue ($T-Nb_2O_5$), it can be synthesized in less extreme conditions, which favors nano-structuring and scale-up.[39,46,47] By synthetically combining $TT-Nb_2O_5$ and high-conductivity multiwalled carbon nano-tubes (MWCNTs), strongly bound together with a glucose-derived carbon to form a well-integrated composite electrode, the conductivity, mechanical strength, stability, and specific capacity of the anode material were optimized. The needle-like Nb_2O_5@CNT composites have delivered a high reversible specific capacity of 170 mAh g^{-1} at 0.2 A g^{-1} and excellent rate retention when compared to $T-Nb_2O_5$-based KIB systems to date: 102 mAh g^{-1} at 2 A g^{-1} and 72 mAh g^{-1} at 5 A g^{-1}. This therefore offers a scalable solution to the development of sustainable high-rate energy storage systems.

2. METHODOLOGY

2.1. Synthesis of Nb_2O_5/g-CNT Composites. Nb_2O_5@CNT was synthesized using a one-step hydrothermal method followed by annealing. 0.4 g of ammonium niobate oxalate hydrate, 35 mg of multiwalled carbon nanotubes (outer diameter × inner diameter × length = 10 ± 1 nm × 4.5 ± 0.5 nm × 3 to ∼6 μm; Sigma-Aldrich, U.K.), and 0.4 g of glucose (Sigma-Aldrich, U.K.) were uniformly mixed and ground with a mortar and pestle before they were dispersed into 30 mL of methanol/DI water (1:1 in volume ratio). The homogeneous suspension was transferred to a Teflon-lined autoclave (4744 Acid Digestion Vessel, Parr) and heated in an oven at 180 °C

for 12 h while the hydrothermal reaction proceeded. The as-synthesized powder was washed with DI water and freeze-dried (PowerDry LL3000, Thermo Scientific, U.K.) before being annealed at 500 °C for 3 h in an argon atmosphere using a tube furnace. The same methodology was applied for the synthesis of pure Nb_2O_5 without the addition of MWCNTs and glucose. Similarly, the glucose-derived carbon/MWCNT composite (g-CNT) was synthesized by mixing MWCNT and glucose as above and treating them under the same hydrothermal and annealing conditions.

2.2. Material Characterization. The crystal structure and phase of the as-received powder samples were analyzed by powder X-ray diffraction (XRD, STOE SEIFERT, Cu foil mode). The surface chemistry of the samples was analyzed by X-ray photoelectron spectroscopy (XPS, Thermo-Scientific, K-alpha photoelectron spectrometer), and the data were processed using CASA XPS with calibration of the binding energy position with C 1s at 284.8 eV. The surface area and pore size of the composite were analyzed by N_2 adsorption−desorption measurements (Micromeritics, Flex&3Flex). The morphology of the Nb_2O_5@CNT powder was analyzed by scanning electron microscopy (SEM, JOEL JSM6701 FEG-SEM), and the chemical structure of the materials was further analyzed by Raman spectroscopy (laser wavelength of ∼540 nm, DXR3 Raman Microscope). Elemental analysis of the composite was conducted by energy-dispersive spectroscopy (EDS, Oxford INCA X-act). The bulk composition of each sample was determined by thermogravimetric analysis (TGA, Mettler Toledo, TGA/DSC 3+).

2.3. Electrochemical Characterization. Nb_2O_5@CNT and Nb_2O_5 anodes were prepared by mixing homogeneous slurries of the active material, carbon black (Sigma-Aldrich, U.K.), and poly(vinylidene fluoride) (PVDF, MTI, U.K.) in N-methyl-2-pyrrolidoone (NMP, Sigma-Aldrich U.K.) in a weight ratio of 7:2:1 using a Thinky mixer (Thinky ARE-250). The slurry was then coated onto a 25 μm thick aluminum current collector via doctor blading. After drying in a vacuum oven (Binder, U.K.) for 12 h at 120 °C, the electrodes were cut to a diameter of 16 mm and assembled into CR2032 coin cells in an argon-filled glovebox at room temperature (∼25 °C) with a glass fiber separator (Whatman GF/D), 90 μL of potassium bis(fluorsulfonyl)imide (KFSI, Combi-Blocks, US) in ethylene carbonate (EC)/diethyl carbonate (DEC) (1:1 in volume ratio, Sigma-Aldrich, U.K.) as the electrolyte, and potassium foil (Sigma-Aldrich, U.K.) as the counter electrode. Cyclic voltammetry (CV) tests were conducted using the Biologic battery cycler (Biologic BCS-800) within 0.01 and 3 V (vs K/K$^+$) at scan rates between 0.1 and 2 mV s^{-1}. The charge−discharge (CD) performances of Nb_2O_5@CNT and Nb_2O_5 were also analyzed using a battery cycler in the potential window of 0.01−3.0 V (vs K/K$^+$) at current densities between 0.1 and 5 A g^{-1}. Electrochemical impedance spectroscopy (EIS) was conducted using a Biologic potentiostat (Biologic VSP-300) with an amplitude of 10 mV in the frequency range of 100 kHz to 0.1 mHz.

3. RESULTS AND DISCUSSION

Pseudohexagonal Nb_2O_5, glucose-derived-carbon-decorated multiwalled carbon nanotubes (gCNT), and their composites (Nb_2O_5@CNT) were synthesized via a one-step hydrothermal method and post-annealing (see Figure S1, Supporting Information). The XRD patterns of Nb_2O_5@CNT, gCNT, and Nb_2O_5 are shown in Figure 1a. Characteristic peaks for the
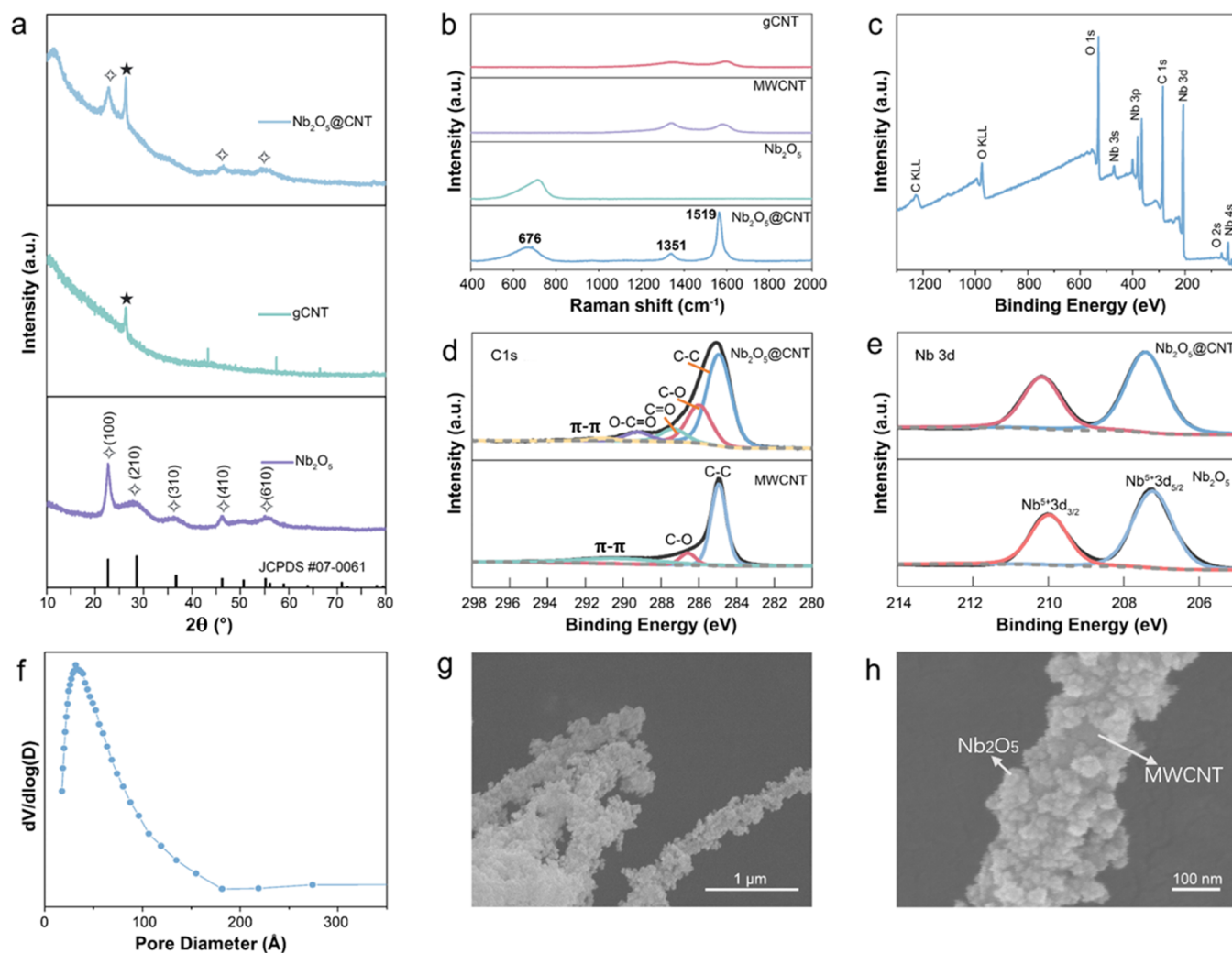
**Figure 1.** (a) XRD patterns of Nb_2O_5@CNT, Nb_2O_5, and gCNT. (b) Raman spectra of Nb_2O_5@CNT, Nb_2O_5, MWCNT, and gCNT. (c) XPS survey spectrum of Nb_2O_5@CNT. (d) C 1s XPS spectra of Nb_2O_5@CNT and MWCNT. (e) Nb 3d spectra of Nb_2O_5@CNT and Nb_2O_5. (f) Pore size distribution of Nb_2O_5@CNT. (g, h) SEM images of Nb_2O_5@CNT.

(100), (210), (310), (400), and (610) reflections can be observed for Nb_2O_5, which can be assigned to the pseudohexagonal form of Nb_2O_5 (TT- Nb_2O_5, JCPDS #07-0061). TT-Nb_2O_5 has a crystal structure similar to that of T-Nb_2O_5, but it consists of distorted sub-cells with a pseudohexagonal symmetry in a superlattice.[39,46] The diffraction pattern of gCNT shows the typical (002) plane of CNTs at $2\theta \approx 26°$, and the Nb_2O_5@CNT pattern can be interpreted as a combination of the contributions from TT-Nb_2O_5 and gCNT.[48] The particle size of Nb_2O_5 within Nb_2O_5@CNT was estimated by the Scherrer equation (see eq S1) to be ~8.47 nm. As the amorphous-glucose-derived carbon could not be detected via XRD, the overall composition of Nb_2O_5@CNT was analyzed by thermogravimetric analysis (TGA) (see Figure S2, Supporting Information). The mass loss of 3.21% at 230 °C can be attributed to the removal of absorbed water. The further losses of 21.33 and 21.32% at 261 and 571 °C can be attributed to the combustion of amorphous carbon and MWCNTs in the sample, respectively, leaving a 54.14% remainder due to residual Nb_2O_5. Hence, the overall Nb_2O_5-to-carbon ratio in the Nb_2O_5@CNT composite was close to 1.3:1.

Raman spectroscopy of Nb_2O_5@CNT was then performed to provide insights into the nature of the amorphous glucose-derived carbon (Figure 1b). The peaks centered at 676, 1351, and 1519 cm^{-1} correspond to vibrations of the Nb−O bonds, sp^3 carbons (D-band), and graphitic carbons (G-band), respectively.[41,49−51] In contrast to the Raman spectrum of pristine MWCNT, the intensity of graphitic carbon (G-band) is significantly higher than that of the disordered carbon (D-band) for Nb_2O_5@CNT, which may suggest that the hydrothermal treatment reduced the defect density in the framework of MWCNTs.[52] Interestingly, this effect was not observed for gCNT, which was prepared using an equivalent hydrothermal method. This phenomenon may be caused by the surface-enhanced Raman scattering (SERS)-active performance of Nb_2O_5. Nb_2O_5 is a semiconductor with a high refraction index of 2.31, which means that the Mie resonance-generated light can be easily excited by Nb_2O_5 and lead to enhanced surface electric and magnetic fields.[53] In addition, TT-Nb_2O_5 nanoparticles in the Nb_2O_5@CNT composite have rich surface active sites (Lewis sites and Brønsted sites), which could promote the interaction between Nb_2O_5 and the probe molecules on its surface and result in the enlarged Raman scattering cross section.[53,54] The Raman spectras were further
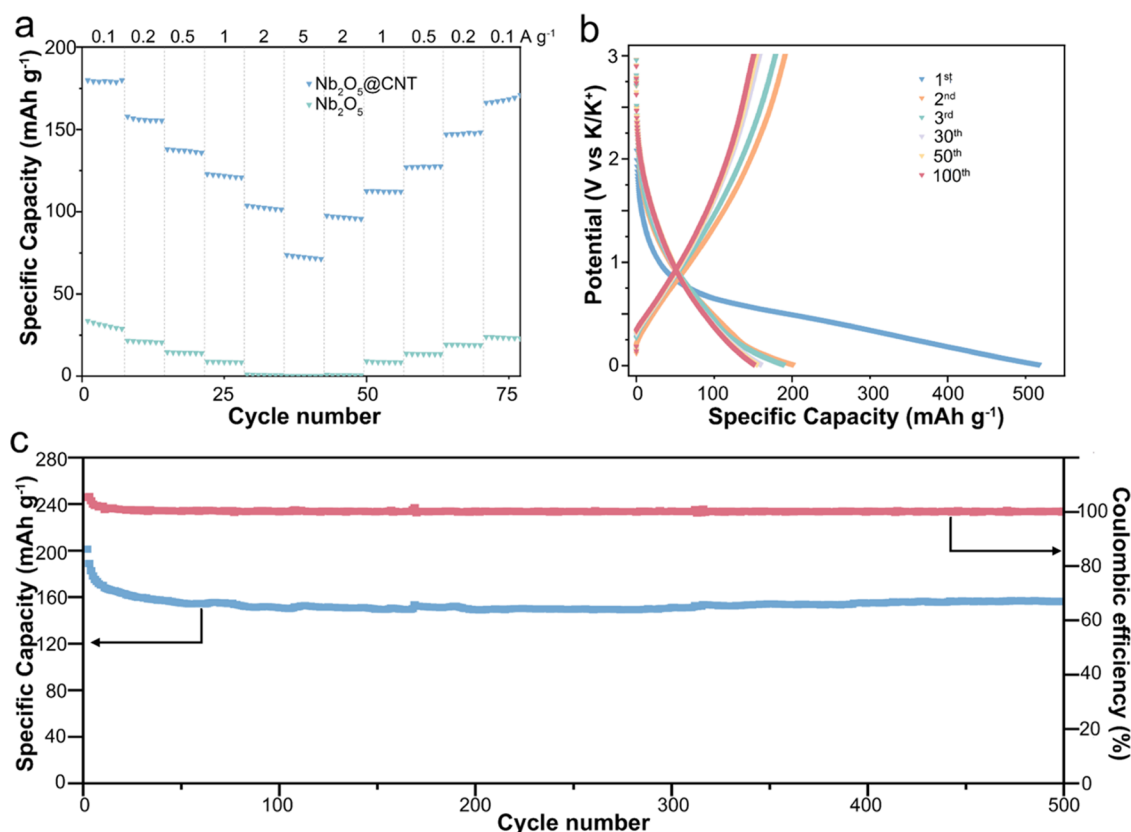
Figure 2. (a) Rate performances of Nb_2O_5@CNT (0.92 mg cm^{-2}) and Nb_2O_5 (0.98 mg cm^{-2}) at increasing current densities of 0.1, 0.2, 0.5, 1, 2, and 5 A g^{-1}. (b) Charge/discharge performance of Nb_2O_5@CNT (1.03 mg cm^{-2}) in the 1st, 2nd, 3rd, 30th, 50th, and 100th cycles at 0.2 A g^{-1}. (c) Cycling performance of Nb_2O_5@CNT (1.03 mg cm^{-2}) at 0.2 A g^{-1}.

processed by peak simulation fitting to study the features of the graphite structure and to analyze defects within the carbon materials (see Figure S3, Supporting Information; D and G in the figure refer to the D and G peaks, respectively, which usually appear near 1350 and 1560 cm^{-1}).[55] By comparing the intensity ratio of the D- and G-bands, the structural perfection can be studied.[56,57] The I_D/I_G values of different materials were calculated to evaluate the defects of the structure and domain size of the carbon materials. The I_D/I_G values of gCNT, MWCNT, and Nb_2O_5@CNT are 2.68, 1.69, and 0.17 accordingly, which indicates that the defect concentration was decreased after hydrothermal synthesis with the addition of Nb_2O_5. This, together with the Raman results, further confirmed the coexistence of Nb_2O_5, glucose-derived amorphous carbon, and MWCNTs and confirmed the high purity of the composite.

X-ray photoelectron spectroscopy (XPS) was used to analyze the surface chemistry of the samples. The XPS survey spectrum of Nb_2O_5@CNT (Figure 1c) shows no peaks for elements other than Nb, C, and O, as expected, further confirming its high purity. Comparisons of the Nb 3d and C 1s regions of Nb_2O_5@CNT, Nb_2O_5, and MWCNT are shown in Figure 1d,e. Nb^{5+} $3d_{5/2}$ and Nb^{5+} $3d_{3/2}$ peaks for Nb_2O_5@CNT can be found at 207.44 and 210.18 eV, which show no obvious change when compared to pure Nb_2O_5. This result illustrated that the hydrothermal reaction with the addition of MWCNT and glucose did not change the chemical state of Nb_2O_5.

Regarding the carbon contribution, the peak at 284.9 eV for MWCNT C 1s, which corresponds to the C—C bond in the

carbon skeleton, was found to be broader in the C 1s of Nb_2O_5@CNT due to the addition of glucose-derived carbon. Besides this, peaks that can be assigned to C—O, C=O, and O—C=C bonds at 285.98, 287.34, and 289.23 eV can also be seen, which suggest that the glucose-derived carbon in the composite contains surface functional groups[55] that may provide binding sites for Nb_2O_5 to anchor to the carbon framework. The atomic percentages of components of different chemical states are shown in Table S1. In the fitted C 1s spectrum of Nb_2O_5@CNT, 59.59 atom % of the C—C bonds (peak at 284.93 eV) are attributed to the bonding between MWCNT and glucose-derived carbon, whereas 22.74 atom % C—O, 8.31 atom % C=O, and 5.84 atom % O—C=O bonds are related to the functional groups of glucose-derived carbon.

The surface area and pore distribution of the Nb_2O_5@CNT composite were analyzed by N_2 adsorption/desorption measurements at 77K (Figure S4, Supporting Information). The result shows a Brunauer−Emmett−Teller (BET) surface area of 519.75 m^2 g^{-1} and a Barrett−Joyner−Halenda (BJH) average pore diameter of 64.57 Å (Figure 1f). The high surface area of the composite was achieved due to the combination of nanosized particles and their even distribution on CNTs. The N_2 adsorption/desorption isotherm confirmed that the composite is mesoporous.[58] The morphology of Nb_2O_5@CNT was further investigated by scanning electron microscopy (SEM; Figures 1g,h and S5, Supporting Information), which showed a needle-like structure consisting of Nb_2O_5 NPs uniformly coated on supporting MWCNTs, further confirmed by EDS (Figure S6, Supporting Information). Moreover, uneven distribution of Nb_2O_5 can be found in the SEM image
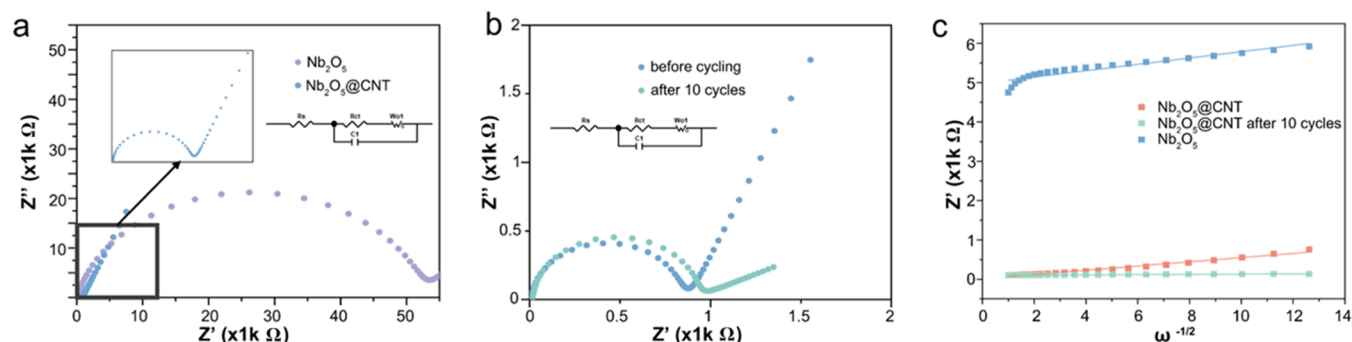
Figure 3. EIS plots of (a) Nb_2O_5@CNT and Nb_2O_5 and (b) Nb_2O_5@CNT before cycling and after 10 cycles. (c) Randles plot of the electrodes of Nb_2O_5, Nb_2O_5@CNT, and Nb_2O_5@CNT after 10 cycles in the Warburg region.

of the Nb_2O_5@CNT composite with low carbon content (Figure S7, Supporting Information), which indicates that controlling the carbon content is extremely important in achieving a uniform structure of the composite. This high-surface-area nanostructure should provide enhanced electrical conductivity, good structural flexibility, and fast mass transport, thereby maximizing the capacity, rate performance, and stability of the composite when utilized as a KIB anode.

Figure 2 shows the electrochemical performance of Nb_2O_5@ CNT as the active anode material in a KIB half-cell. The theoretical capacity of Nb_2O_5@CNT is 387 mAh g^{-1}. The rate performance of Nb_2O_5@CNT and Nb_2O_5 are compared in Figure 2a; Nb_2O_5@CNT delivers capacities of 179, 156, 137, 121, 102, and 72 mAh g^{-1} at current densities of 0.1, 0.2, 0.5, 1, 2, and 5 A g^{-1} (from ~0.3C to ~15C) respectively, showing ~5 times higher capacity compared to that of pure Nb_2O_5 at low rates during long cycles (see Figure S8, Supporting Information) and an order of magnitude higher capacities at high rates. The performance of Nb_2O_5@CNT at high rates is better than those of all Nb_2O_5-based KIB anodes in the literature to date (see Figure S9, Supporting Information). Moreover, these capacities are recoverable when the current density is decreased stepwise from 5 to 0.1 A g^{-1}.

To understand the impact of the hydrothermally prepared carbon framework for TT-Nb_2O_5, the rate performance of Nb_2O_5@CNT with half the Nb_2O_5 content (0.2Nb_2O_5@ CNT) and a simple mixture of MWCNT and TT-Nb_2O_5 was also tested (see Figure S10, Supporting Information). The 0.2Nb_2O_5@CNT delivered specific capacities of 98, 68, 42, 24, 5, and 0.3 mAh g^{-1} at current densities of 0.1, 0.2, 0.5, 1, 2, and 5 A g^{-1}, indicating that the capacity of Nb_2O_5@CNT is mainly bestowed by TT-Nb_2O_5 (see Figure S11, Supporting Information). The mixture of MWCNT and TT-Nb_2O_5 delivered specific capacities of only 31, 21, 14, 9, 1, and 0.1 mAh g^{-1} as the current density was increased from 0.1 to 5 A g^{-1}, showing that the glucose-derived carbon plays a vital role in achieving the capacity of the composite. The intimately linked structure is expected to significantly improve electrical conductivity and mass transport while offering mechanical stabilization.

Similar to other transition metal oxides, Nb_2O_5@CNT exhibited a relatively low first-cycle Coulombic efficiency (FCCE) of 38.9% (Figure 2b), which can be attributed to the formation of a solid electrolyte interface (SEI). However, after the first cycle, the change in the CD profile was minimal, which indicates good electrode and SEI stability at Nb_2O_5@CNT. In fact, the long-term cycling performance at a current density of 0.2 A g^{-1} (Figure 2c) shows that the specific capacity of the

electrode is maintained at ~152 mAh g^{-1} for a minimum of 500 cycles with Coulombic efficiencies close to 100%. A similar lifetime study was also conducted for glucose-coated MWCNTs to evaluate the impact of the carbon base on the composite capacity and stability. As shown in Figure S7, glucose-coated MWCNTs provide a specific capacity of 67 mAh g^{-1}, whereas a simple Nb_2O_5 electrode exhibits a specific capacity of 12 mAh g^{-1} at 0.2 A g^{-1}, demonstrating that the designed composite offers significant benefits over its constituent parts.

Electrochemical impedance spectroscopy (EIS) measurements were conducted to confirm the differences in charge transfer and inherent resistance between Nb_2O_5@CNT and Nb_2O_5 (Figure 3a). Equivalent circuit models for both spectra are shown in Figure 3a,b, in which R_s and R_{ct} represent the ohmic resistance between the electrolyte/surface and charge-transfer resistance, respectively.[59] The measured R_{ct} of Nb_2O_5@CNT was found to be 790 Ω, which is ~66 times smaller than that of Nb_2O_5 (52 kΩ). The huge decrease in R_{ct} can be attributed to the addition of the MWCNT framework, which lowers the energy barrier for electron transfer in the composite. The Nyquist plot of Nb_2O_5@CNT before cycling was also compared with the equivalent after 10 cycles at 0.2 A g^{-1} (Figure 3b). The small increase in the diameter of the semicircle after 10 cycles can be attributed to the formation of an SEI film, which increases the charge-transfer resistance of the battery system. However, the magnitude is indicative of a compact and stable interface. The slope at low frequencies, corresponding to the Warburg impedance, is indicative of the K ion diffusion in the cell.[60−62]

To further study the capacitance behavior, the K-ion diffusion coefficient was calculated using the EIS data based on eq 1[63]

$$D_{K^+} = \frac{R^2 T^2}{2A^2 n^4 F^4 c^2 \sigma^2} \qquad (1)$$

where D_{K^+} is the diffusion coefficient, R is the gas constant (8.314 J mol^{-1} K^{-1}), T is the absolute temperature, A is the effective working area of the anode, n is the number of electrons transferred, F is the Faraday constant (96 500 C mol^{-1}), C is the K concentration, and σ is the Warburg factor. The Warburg factor can be calculated by the linear Randles equation (eq 2)[64]

$$Z' = R_s + R_{ct} + \sigma \omega^{-1/2} \qquad (2)$$

where ω in the angular frequency at low frequencies. As shown in Figure 3c, the slope of the simulated linear plots
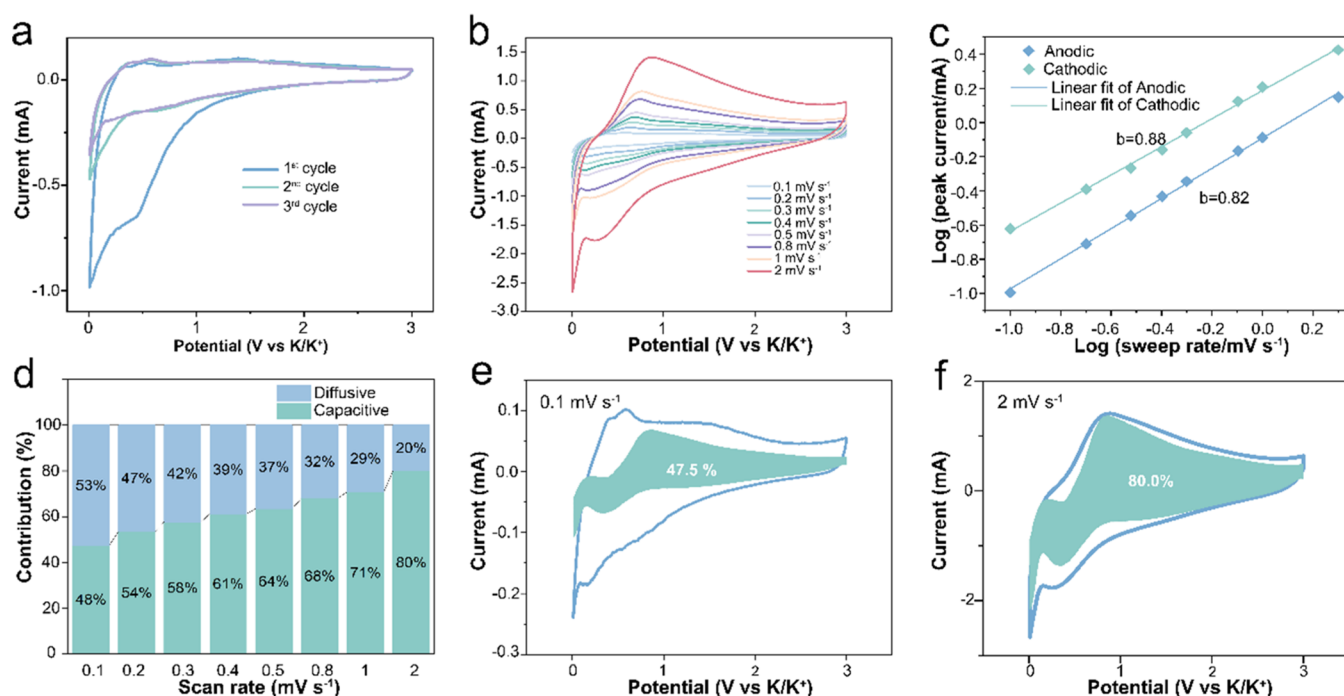
Figure 4. (a) First three CV cycles of Nb$_2$O$_5$@CNT at 0.1 mV s^{-1}. (b) CV profiles of Nb$_2$O$_5$@CNT at different scan rates from 0.1 to 2 mV s^{-1}. (c) Logarithmic relationship between the peak current and scan rates. (d) Contribution ratio of capacitive and diffusive reactions to the capacity of Nb$_2$O$_5$@CNT at different scan rates. Fitting of the pseudocapacitive contribution at (e) 0.1 and (f) 2 mV s^{-1}.

represents the Warburg factor (807.12, 536.88, and 31.38 Ω S$^{-1/2}$ for Nb$_2$O$_5$ and Nb$_2$O$_5$@CNT before cycling and Nb$_2$O$_5$@CNT after 10 cycles, respectively). Consequently, the K-ion diffusion coefficients can be calculated to be 1.76 × 10^{-14}, 3.97 × 10^{-14}, and 1.16 × 10^{-11} cm^2 s^{-1} for Nb$_2$O$_5$ and Nb$_2$O$_5$@CNT before cycling and Nb$_2$O$_5$@CNT after 10 cycles, respectively. The higher diffusion rate of Nb$_2$O$_5$@CNT after 10 cycles compared with the other two is because of the capacitance behavior of the anode before the exhibition of electrochemical reaction after SEI formation, which justifies its outstanding rate performance.[15]

To uncover the charge storage mechanism of Nb$_2$O$_5$@CNT in KIBs, cyclic voltammetry (CV) tests were conducted. The initial three CV cycles at 0.1 mV s^{-1} are shown in Figure 4a. The broad peak centered at 0.45 V, which is the dominant feature of the first cathodic scan, can be assigned to the formation of the SEI layer, caused by the irreversible decomposition of the KFSI-based electrolyte in the first cycle;[65] this peak disappears by the 3rd cycle, which is important as it indicates the formation of a stable SEI. Interestingly, at low scan rates, few other faradic peaks can be resolved, but as shown in Figure 4b, the CV profile for Nb$_2$O$_5$@CNT changed as the scan rate was increased from 0.1 to 2 mV s^{-1}. Two broad peaks, which correspond to the reaction Nb$_2$O$_5$ + xK$^+$ ⇌ K$_x$Nb$_2$O$_5$, become increasingly resolvable at higher scan rates while the distance between anodic and cathodic peaks increases, indicating an increase in the degree of polarization. To further reveal the mechanism of the potassiation/de-potassiation, the ex-situ XPS profile of cycled Nb$_2$O$_5$@CNT was studied. As the SEI layer formed on the surface of the cycled nanostructured anode, most of the contribution from the underlying electrodes was blocked. However, the mechanism can still be studied by comparing the changes in peak shifts at charge/discharge states in the XPS spectrum. As shown in Figure S12a,b, the decrease in the

intensity of the C−C bond in the C 1s fitting is coupled with an increase in the intensities of K 2p peaks after discharge, which indicates the intercalation of K-ions and the formation of potassium−carbon compounds.[66] The Nb 3d spectra indicates the reversible oxidation and reduction of Nb species in the fully charged and discharged states (see Figure SI12c,d, Supporting Information). The change in the intensity of Nb^{5+}, which corresponds to the change in the intensity of Nb−O in the O 1s spectra, indicates that Nb^{5+} is reduced to lower valence states after discharge.[67]

Figure 4c shows the logarithmic relationship between the peak current of the cathodic and anodic processes (i) and scan rate (v), from which the capacitive contribution of Nb$_2$O$_5$@CNT can be determined by the power law[68,69]

$$i = av^b \tag{3}$$

where a and b are variable parameters. The b-value, which is the slope of the linear fit (Figure 4c), can be used to determine the Faradic and non-Faradic behaviors in the electrochemical process of Nb$_2$O$_5$@CNT. When the b-value is equal to 0.5, the electrochemical process is regarded as being controlled by a diffusion-controlled behavior, but if the b-value is close to 1, it is assumed to be dominated by a pseudocapacitive behavior.[70] The b-values of Nb$_2$O$_5$@CNT were calculated to be 0.88 and 0.82 for the anodic and cathodic peaks, respectively, suggesting primarily pseudocapacitive storage in Nb$_2$O$_5$@CNT-based KIBs, indicating its fast kinetics. The contributions of diffusive and capacitive behaviors to the total capacity can be further analyzed quantitatively using eq 4[71]

$$i(v) = k_1v + k_2v^{1/2} \tag{4}$$

where (k$_1$v) represents the capacitive contribution and (k$_2$v$^{1/2}$) signifies the diffusive dominance. This calculation reveals that 48, 54, 56, 61, 64, 68, 71, and 80% of the capacity of Nb$_2$O$_5$@CNT were provided by (pseudo)capacitive reactions at scan

rates of 0.1, 0.2, 0.3, 0.4, 0.5, 0.8, 1.0, and 2.0 mV s^{-1}, respectively (Figure 4d). The capacitive contribution ratio increases with the increasing scan rate (Figure 4e,f), consistent with the high rate capability of Nb$_2$O$_5$@CNT, indicating that the high accessibility of the electrically connected Nb$_2$O$_5$ can lead to very fast redox reactions.

4. CONCLUSIONS

In summary, a composite of needle-like pseudohexagonal Nb$_2$O$_5$ on MWCNT was synthesized by a scalable hydrothermal method and studied as an anode for KIBs. Nb$_2$O$_5$@CNT exhibited a highly reversible specific capacity (179 mAh g^{-1}) and excellent cyclability both in terms of long cycles (152 mAh g^{-1} at 0.2 A g^{-1} after 500 cycles) and at high rates (72 mAh g^{-1} at 0.5 A g^{-1}). All of these metrics are the best for all reported Nb$_2$O$_5$-based KIB anodes to date. The enhanced electrochemical performance is attributed to the optimization of electron/ion diffusion kinetics, electrical conductivity, and mechanical stability offered by the composite. Importantly, this work therefore offers a scalable route for the production of a high-activity post-lithium-ion battery anode material, with significant implications for next-generation energy storage systems. With optimization, the material demonstrated could enhance the commercial viability of KIBs.

■ ASSOCIATED CONTENT

Ⓢ Supporting Information

The Supporting Information is available free of charge at https://pubs.acs.org/doi/10.1021/acsami.2c21490.

Schematic of the formation of the Nb$_2$O$_5$@CNT composite (Figure S1); TGA curve of Nb$_2$O$_5$@CNT (Figure S2); atomic percentage calculated by processing the fitted Nb 3d, C 1s, and O 1s XPS spectra (Table S1); Raman spectra of Nb$_2$O$_5$@CNT, Nb$_2$O$_5$ and gCNT (Figure S3); N$_2$ adsorption/desorption isotherm of Nb$_2$O$_5$@CNT (Figure S4); TEM image of the Nb$_2$O$_5$@CNT composite (Figure S5); EDS profile of the Nb$_2$O$_5$@CNT composite (Figure S6); SEM image of Nb$_2$O$_5$@0.5CNT (Figure S7); CD profiles of Nb$_2$O$_5$@CNT (0.94 mg cm^{-2}), g-MWCNT (0.81 mg cm^{-2}), and Nb$_2$O$_5$ (0.96 mg cm^{-2}) at 0.2 A g^{-1} (Figure S8); Comparison of Nb$_2$O$_5$@CNT composite in this paper with other reported Nb$_2$O$_5$-based KIB anode (Figure S9); Rate performance of pure Nb$_2$O$_5$ and mixture of Nb$_2$O$_5$ and MWCNT at different current densities (Figure S10); rate performance of 0.4Nb$_2$O$_5$@CNT (low carbon content) and 0.2Nb$_2$O$_5$@CNT (high carbon content) in KIBs (Figure S11) (PDF)

■ AUTHOR INFORMATION

Corresponding Authors

Guanjie He − Electrochemical Innovation Lab, Department of Chemical Engineering, UCL, London WC1E 7JE, U.K.; Ⓞ orcid.org/0000-0002-7365-9645; Email: g.he@ucl.ac.uk

Thomas S. Miller − Electrochemical Innovation Lab, Department of Chemical Engineering, UCL, London WC1E 7JE, U.K.; Ⓞ orcid.org/0000-0002-2224-5768; Email: T.Miller@ucl.ac.uk

Authors

Guanxu Chen − Electrochemical Innovation Lab, Department of Chemical Engineering, UCL, London WC1E 7JE, U.K.

Jintao Chen − Electrochemical Innovation Lab, Department of Chemical Engineering, UCL, London WC1E 7JE, U.K.

Siyu Zhao − Electrochemical Innovation Lab, Department of Chemical Engineering, UCL, London WC1E 7JE, U.K.

Complete contact information is available at:
https://pubs.acs.org/10.1021/acsami.2c21490

Author Contributions

G.C. was responsible for the design of the project, experiments for synthesis, material characterization, electrochemical characterization, and writing of the manuscript. J.C. conducted the XPS. S.Z. conducted the Raman spectroscopy. T.S.M. and G.H. supervised the project. All authors contributed to the review of the manuscript.

Notes

The authors declare no competing financial interest.

■ ACKNOWLEDGMENTS

■ REFERENCES

(1) Goodenough, J. B. Evolution of Strategies for Modern Rechargeable Batteries. *Acc. Chem. Res.* **2013**, *46*, 1053−1061.

(2) Tarascon, J. M. Is Lithium the New Gold? *Nat. Chem.* **2010**, *2*, 510.

(3) Sun, Y.; Zhu, D.; Liang, Z.; Zhao, Y.; Tian, W.; Ren, X.; Wang, J.; Li, X.; Gao, Y.; Wen, W.; Huang, Y.; Li, X.; Tai, R. Facile Renewable Synthesis of Nitrogen/Oxygen Co-Doped Graphene-like Carbon Nanocages as General Lithium-Ion and Potassium-Ion Batteries Anode. *Carbon* **2020**, *167*, 685−695.

(4) John, B.; Anoopkumar, V.; Mercy, T. D. Potassium-Ion Batteries: Key to Future Large-Scale Energy Storage? *ACS Appl. Energy Mater.* **2020**, *3*, 9478−9492.

(5) Zheng, J.; Wu, Y.; Sun, Y.; Rong, J.; Li, H.; Niu, L. Advanced Anode Materials of Potassium Ion Batteries: From Zero Dimension to Three Dimensions. *Nano-Micro Lett.* **2020**, *13*, No. 12.

(6) Min, X.; Xiao, J.; Fang, M.; Wang, W.; Zhao, Y.; Liu, Y.; Abdelkader, A. M.; Xi, K.; Kumar, R. V.; Huang, Z. Potassium-Ion Batteries: Outlook on Present and Future Technologies. *Energy Environ. Sci.* **2021**, *14*, 2186−2243.

(7) Ma, L.; Lv, Y.; Wu, J.; Xia, C.; Kang, Q.; Zhang, Y.; Liang, H.; Jin, Z. Recent Advances in Anode Materials for Potassium-Ion Batteries: A Review. *Nano Res.* **2021**, *14*, 4442−4470.

(8) Fan, L.; Ma, R.; Zhang, Q.; Jia, X.; Lu, B. Graphite Anode for a Potassium-Ion Battery with Unprecedented Performance. *Angew. Chem.* **2019**, *131*, 10610−10615.

(9) Zhang, W.; Mao, J.; Li, S.; Chen, Z.; Guo, Z. Phosphorus-Based Alloy Materials for Advanced Potassium-Ion Battery Anode. *J. Am. Chem. Soc.* **2017**, *139*, 3316−3319.

(10) Kishore, B.; Venkatesh, G.; Munichandraiah, N. K$_2$Ti$_4$O$_9$: A Promising Anode Material for Potassium Ion Batteries. *J. Electrochem. Soc.* **2016**, *163*, A2551−A2554.

(11) Jian, Z.; Hwang, S.; Li, Z.; Hernandez, A. S.; Wang, X.; Xing, Z.; Su, D.; Ji, X. Hard−Soft Composite Carbon as a Long-Cycling and High-Rate Anode for Potassium-Ion Batteries. *Adv. Funct. Mater.* **2017**, *27*, No. 1700324.

(12) Bi, H.; He, X.; Yang, L.; Li, H.; Jin, B.; Qiu, J. Interconnected Carbon Nanocapsules with High N/S Co-Doping as Stable and High-Capacity Potassium-Ion Battery Anode. *J. Energy Chem.* **2022**, *66*, 195−204.

(13) Xiao, W.; Li, X.; Cao, B.; Huang, G.; Xie, C.; Qin, J.; Yang, H.; Wang, J.; Sun, X. Constructing High-Rate and Long-Life Phosphorus/Carbon Anodes for Potassium-Ion Batteries through Rational Nanoconfinement. *Nano Energy* **2021**, *83*, No. 105772.

(14) Qiao, F.; Wang, J.; Zhu, Y.; Tan, X.; Wang, X.; An, Q. Cheese-like Porous SnP2O7 Composite as a Long-Life and High-Rate Anode Material for Potassium-Ion Batteries. *Chem. Eng. J.* **2022**, *439*, No. 135777.

(15) Kishore, B.; Venkatesh, G.; Munichandraiah, N. K2Ti4O9: A Promising Anode Material for Potassium Ion Batteries. *J. Electrochem. Soc.* **2016**, *163*, A2551−A2554.

(16) Liang, Y.; Luo, C.; Wang, F.; Hou, S.; Liou, S.-C.; Qing, T.; Li, Q.; Zheng, J.; Cui, C.; Wang, C. An Organic Anode for High Temperature Potassium-Ion Batteries. *Adv. Energy Mater.* **2019**, *9*, No. 1802986.

(17) Lübke, M.; Sumboja, A.; Johnson, I. D.; Brett, D. J. L.; Shearing, P. R.; Liu, Z.; Darr, J. A. High Power Nano-Nb2O5 Negative Electrodes for Lithium-Ion Batteries. *Electrochim. Acta* **2016**, *192*, 363−369.

(18) Qu, X.; Liu, Y.; Li, B.; Xing, B.; Huang, G.; Zhang, C.; Hong, S. W.; Yu, J.; Cao, Y. Synthesis of High Reversibility Anode Composite Materials Using T-Nb2O5 and Coal-Based Graphite for Lithium-Ion Battery Applications. *Energy Fuels* **2020**, *34*, 3887−3894.

(19) Liu, M.; Yan, C.; Zhang, Y. Fabrication of Nb2O5 Nanosheets for High-Rate Lithium Ion Storage Applications. *Sci. Rep.* **2015**, *5*, No. 8326.

(20) Zhao, Y.; Li, X.; Yan, B.; Xiong, D.; Li, D.; Lawes, S.; Sun, X. Recent Developments and Understanding of Novel Mixed Transition-Metal Oxides as Anodes in Lithium Ion Batteries. *Adv. Energy Mater.* **2016**, *6*, No. 1502175.

(21) Han, X.; Russo, P. A.; Goubard-Bretesché, N.; Patanè, S.; Santangelo, S.; Zhang, R.; Pinna, N. Exploiting the Condensation Reactions of Acetophenone to Engineer Carbon-Encapsulated Nb2O5 Nanocrystals for High-Performance Li and Na Energy Storage Systems. *Adv. Energy Mater.* **2019**, *9*, No. 1902813.

(22) Zhang, Y.; Fang, L. In *A Novel Synthesis of Nb2O5@N-CNF Nanocomposite as Anode Material for Superior Sodium Storage*, IOP Conference Series: Earth and Environmental Science, 2020; Vol. 6191, p 012015.

(23) Kim, H.; Lim, E.; Jo, C.; Yoon, G.; Hwang, J.; Jeong, S.; Lee, J.; Kang, K. Ordered-Mesoporous Nb2O5/Carbon Composite as a Sodium Insertion Material. *Nano Energy* **2015**, *16*, 62−70.

(24) She, L.; Zhang, F.; Jia, C.; Kang, L.; Li, Q.; He, X.; Sun, J.; Lei, Z.; Liu, Z. H. Electrospun Nb2O5 Nanorods/Microporous Multi-channel Carbon Nanofiber Film Anode for Na+ Ion Capacitors with Good Performance. *J. Colloid Interface Sci.* **2020**, *573*, 1−10.

(25) Li, Y.; Wang, H.; Wang, L.; Mao, Z.; Wang, R.; He, B.; Gong, Y.; Hu, X. Mesopore-Induced Ultrafast Na+-Storage in T-Nb2O5/Carbon Nanofiber Films toward Flexible High-Power Na-Ion Capacitors. *Small* **2019**, *15*, No. 1804539.

(26) Jia, R.; Jiang, Y.; Li, R.; Chai, R.; Lou, Z.; Shen, G.; Chen, D. Nb2O5 Nanotubes on Carbon Cloth for High Performance Sodium-Ion Capacitors. *Sci. China Mater.* **2020**, *63*, 1171−1181.

(27) Zhang, Y.; Fang, L.; Sun, W.; Shi, B.; Chen, X.; Gu, Y.; Ding, K.; Wang, Z.; Sun, K. A Novel Synthesis of Nb2O5@rGO Nanocomposite as Anode Material for Superior Sodium Storage. *Chin. Chem. Lett.* **2021**, *32*, 1144−1148.

(28) Subramanian, Y.; Veerasubramani, G. K.; Park, M.-S.; Kim, D.-W. Core-Shell Structured Nb2O5@N-Doped Carbon Nanoparticles as an Anode Material for Na-Ion Batteries. *Mater. Lett.* **2022**, *314*, No. 131891.

(29) Chen, G.; Chen, J.; Parkin, I. P.; He, G.; Miller, T. S. Pseudohexagonal Nb2O5 Decorated Carbon Nanotubes as a High-performance Composite Anode for Sodium-ion Batteries. *ChemElectroChem* **2022**, *9*, No. e202200800.

(30) Meng, J.; He, Q.; Xu, L.; Zhang, X.; Liu, F.; Wang, X.; Li, Q.; Xu, X.; Zhang, G.; Niu, C.; Xiao, Z.; Liu, Z.; Zhu, Z.; Zhao, Y.; Mai, L. Identification of Phase Control of Carbon-Confined Nb2O5 Nanoparticles toward High-Performance Lithium Storage. *Adv. Energy Mater.* **2019**, *9*, No. 1802695.

(31) Li, N.; Zhang, F.; Tang, Y. Hierarchical T-Nb2O5 Nanostructure with Hybrid Mechanisms of Intercalation and Pseudocapacitance for Potassium Storage and High-Performance Potassium Dual-Ion Batteries. *J. Mater. Chem. A* **2018**, *6*, 17889−17895.

(32) Yuan, J.; Li, X.; Liu, J.; Zuo, S.; Li, X.; Li, F.; Gan, Y.; He, H.; Xu, X.; Zhang, X.; Meng, J. Pomegranate-like Structured Nb2O5/Carbon@N-Doped Carbon Composites as Ultrastable Anode for Advanced Sodium/Potassium-Ion Batteries. *J. Colloid Interface Sci.* **2022**, *613*, 84−93.

(33) Rani, R. A.; Zoolfakar, A. S.; O'Mullane, A. P.; Austin, M. W.; Kalantar-Zadeh, K. Thin Films and Nanostructures of Niobium Pentoxide: Fundamental Properties, Synthesis Methods and Applications. *J. Mater. Chem. A* **2014**, *2*, 15683−15703.

(34) Kim, J. W.; Augustyn, V.; Dunn, B. The Effect of Crystallinity on the Rapid Pseudocapacitive Response of Nb2O5. *Adv. Energy Mater.* **2012**, *2*, 141−148.

(35) Nico, C.; Monteiro, T.; Graça, M. P. F. Niobium Oxides and Niobates Physical Properties: Review and Prospects. *Prog. Mater. Sci.* **2016**, *80*, 1−37.

(36) Li, T.; Liu, K.; Nam, G.; Kim, M. G.; Ding, Y.; Zhao, B.; Luo, Z.; Wang, Z.; Zhang, W.; Zhao, C.; Wang, J.-H.; Song, Y.; Liu, M. A Nonstoichiometric Niobium Oxide/Graphite Composite for Fast-Charge Lithium-Ion Batteries. *Small* **2022**, *18*, No. 2200972.

(37) Kong, L.; Zhang, C.; Wang, J.; Qiao, W.; Ling, L.; Long, D. Free-Standing T-Nb2O5/Graphene Composite Papers with Ultrahigh Gravimetric/Volumetric Capacitance for Li-Ion Intercalation Pseudocapacitor. *ACS Nano* **2015**, *9*, 11200−11208.

(38) Wang, L.; Bi, X.; Yang, S. Partially Single-Crystalline Mesoporous Nb2O5 Nanosheets in between Graphene for Ultrafast Sodium Storage. *Adv. Mater.* **2016**, *28*, 7672−7679.

(39) Kong, L.; Cao, X.; Wang, J.; Qiao, W.; Ling, L.; Long, D. Revisiting Li+ Intercalation into Various Crystalline Phases of Nb2O5 Anchored on Graphene Sheets as Pseudocapacitive Electrodes. *J. Power Sources* **2016**, *309*, 42−49.

(40) Yan, L.; Chen, G.; Sarker, S.; Richins, S.; Wang, H.; Xu, W.; Rui, X.; Luo, H. Ultrafine Nb2O5 Nanocrystal Coating on Reduced Graphene Oxide as Anode Material for High Performance Sodium Ion Battery. *ACS Appl. Mater. Interfaces* **2016**, *8*, 22213−22219.

(41) Qu, X.; Liu, Y.; Li, B.; Xing, B.; Huang, G.; Zhao, H.; Jiang, Z.; Zhang, C.; Hong, S. W.; Cao, Y. Nanostructured T-Nb2O5-Based Composite with Reduced Graphene Oxide for Improved Performance Lithium-Ion Battery Anode. *J. Mater. Sci.* **2020**, *55*, 13062−13074.

(42) Wen, X.; Xiang, K.; Zhu, Y.; Xiao, L.; Liao, H.; Chen, X.; Chen, H. Nb2O5-Decorated Nitrogen-Doped Carbon Nanotube Microspheres for Highly Efficient Sulfur Confinement in Lithium-Sulfur Batteries. *Ind. Eng. Chem. Res.* **2019**, *58*, 8724−8733.

(43) Wang, X.; Li, G.; Chen, Z.; Augustyn, V.; Ma, X.; Wang, G.; Dunn, B.; Lu, Y. High-Performance Supercapacitors Based on Nanocomposites of Nb2O5 Nanocrystals and Carbon Nanotubes. *Adv. Energy Mater.* **2011**, *1*, 1089−1093.

(44) Shi, C.; Xiang, K.; Zhu, Y.; Chen, X.; Zhou, W.; Chen, H. Preparation and Electrochemical Properties of Nanocable-like Nb2O5/Surface-Modified Carbon Nanotubes Composites for Anode Materials in Lithium Ion Batteries. *Electrochim. Acta* **2017**, *246*, 1088−1096.

(45) Shi, C.; Xiang, K.; Zhu, Y.; Chen, X.; Zhou, W.; Chen, H. Preparation and Electrochemical Properties of Nanocable-like Nb2O5/Surface-Modified Carbon Nanotubes Composites for Anode Materials in Lithium Ion Batteries. *Electrochim. Acta* **2017**, *246*, 1088−1096.

(46) Gomes, G. H. M.; Mohallem, N. D. S. Insights into the TT-Nb2O5 Crystal Structure Behavior. *Mater. Lett.* **2022**, *318*, No. 132136.

(47) Ding, H.; Song, Z.; Zhang, H.; Zhang, H.; Li, X. Niobium-Based Oxide Anodes toward Fast and Safe Energy Storage: A Review. *Mater. Today Nano* **2020**, *11*, No. 100082.

(48) Singh, D. K.; Iyer, P. K.; Giri, P. K. Diameter Dependence of Interwall Separation and Strain in Multiwalled Carbon Nanotubes Probed by X-Ray Diffraction and Raman Scattering Studies. *Diamond Relat. Mater.* **2010**, *19*, 1281−1288.

H

(49) She, L.; Yan, Z.; Kang, L.; He, X.; Lei, Z.; Shi, F.; Xu, H.; Sun, J.; Liu, Z. H. Nb2O5 Nanoparticles Anchored on an N-Doped Graphene Hybrid Anode for a Sodium-Ion Capacitor with High Energy Density. *ACS Omega* **2018**, *3*, 15943−15951.

(50) Raba, A. M.; Bautista-Ruíz, J.; Joya, M. R. Synthesis and Structural Properties of Niobium Pentoxide Powders: A Comparative Study of the Growth Process. *Mater. Res.* **2016**, *19*, 1381−1387.

(51) Luo, D.; Ma, C.; Hou, J.; Zhang, Z.; Feng, R.; Yang, L.; Zhang, X.; Lu, H.; Liu, J.; Li, Y.; Zhang, Y.; Wang, X.; Chen, Z. Integrating Nanoreactor with O−Nb−C Heterointerface Design and Defects Engineering Toward High-Efficiency and Longevous Sodium Ion Battery. *Adv. Energy Mater.* **2022**, *12*, No. 2103716.

(52) Hodkiewicz, J. Characterizing Carbon Materials with Raman Spectroscopy. Application Note 51901 Thermo Fisher Scientific: Madison, WI, 2010.

(53) Yang, L.; Wei, Y.; Song, Y.; Peng, Y.; Yang, Y.; Huang, Z. Surface-Enhanced Raman Scattering from Amorphous Nanoflower-Structural Nb2O5 Fabricated by Two-Step Hydrothermal Technology. *Mater. Des.* **2020**, *193*, No. 108808.

(54) Zhao, Y.; Eley, C.; Hu, J.; Foord, J. S.; Ye, L.; He, H.; Tsang, S. C. E. Shape-Dependent Acidity and Photocatalytic Activity of Nb2O5 Nanocrystals with an Active TT (001) Surface. *Angew. Chem.* **2012**, *124*, 3912−3915.

(55) Yuan, L. P.; Wu, Z. Y.; Jiang, W. J.; Tang, T.; Niu, S.; Hu, J. S. Phosphorus-Doping Activates Carbon Nanotubes for Efficient Electroreduction of Nitrogen to Ammonia. *Nano Res* **2020**, *13*, 1376−1382.

(56) Yoon, S.; Lee, S.; Kim, S.; Park, K. W.; Cho, D.; Jeong, Y. Carbon Nanotube Film Anodes for Flexible Lithium Ion Batteries. *J. Power Sources* **2015**, *279*, 495−501.

(57) Thomsen, C.; Reich, S. Double Resonant Raman Scattering in Graphite. *Phys. Rev. Lett.* **2000**, *85*, No. 5214.

(58) Alothman, Z. A. A Review: Fundamental Aspects of Silicate Mesoporous Materials. *Materials* **2012**, *5*, 2874−2902.

(59) Ma, G.; Huang, K.; Ma, J. S.; Ju, Z.; Xing, Z.; Zhuang, Q. C. Phosphorus and Oxygen Dual-Doped Graphene as Superior Anode Material for Room-Temperature Potassium-Ion Batteries. *J. Mater. Chem. A* **2017**, *5*, 7854−7861.

(60) Zhang, E.; Jia, X.; Wang, B.; Wang, J.; Yu, X.; Lu, B. Carbon Dots@rGO Paper as Freestanding and Flexible Potassium-Ion Batteries Anode. *Adv. Sci.* **2020**, *7*, No. 2000470.

(61) Xiong, P.; Bai, P.; Tu, S.; Cheng, M.; Zhang, J.; Sun, J.; Xu, Y. Red Phosphorus Nanoparticle@3D Interconnected Carbon Nanosheet Framework Composite for Potassium-Ion Battery Anodes. *Small* **2018**, *14*, No. 1802140.

(62) Cao, B.; Zhang, Q.; Liu, H.; Xu, B.; Zhang, S.; Zhou, T.; Mao, J.; Pang, W. K.; Guo, Z.; Li, A.; Zhou, J.; Chen, X.; Song, H. Graphitic Carbon Nanocage as a Stable and High Power Anode for Potassium-Ion Batteries. *Adv. Energy Mater.* **2018**, *8*, No. 1801149.

(63) Gao, F.; Tang, Z. Kinetic Behavior of LiFePO4/C Cathode Material for Lithium-Ion Batteries. *Electrochim. Acta* **2008**, *53*, 5071−5075.

(64) Wang, P. P.; Xu, C. Y.; Li, W. D.; Wang, L.; Zhen, L. Low Temperature Electrochemical Performance of β-LixV2O5 Cathode for Lithium-Ion Batteries. *Electrochim. Acta* **2015**, *169*, 440−446.

(65) Jia, X.; Zhang, E.; Yu, X.; Lu, B. Facile Synthesis of Copper Sulfide Nanosheet@Graphene Oxide for the Anode of Potassium-Ion Batteries. *Energy Technol.* **2020**, *8*, No. 1900987.

(66) Qiao, X.; Niu, C.; Liao, D.; Chen, Z.; Sun, L.; Xu, Y. A Self-Growth Strategy for Simultaneous Modulation of Interlayer Distance and Lyophilicity of Graphene Layers toward Ultrahigh Potassium Storage Performance. *Adv. Funct. Mater.* **2021**, *31*, No. 2105145.

(67) Wu, Y.; Fan, X.; Chen, Y.; Gaddam, R. R.; Yu, F.; Xiao, C.; Lin, C.; Zhao, Q.; Sun, X.; Wang, H.; Liu, C.; Li, J.; Zhao, X. S. Fluorine Substitution Enabling Pseudocapacitive Intercalation of Sodium Ions in Niobium Oxyfluoride. *J. Mater. Chem. A* **2019**, *7*, 20813−20823.

(68) Lindström, H.; Södergren, S.; Solbrand, A.; Rensmo, H.; Hjelm, J.; Hagfeldt, A.; Lindquist, S. E. Li+ Ion Insertion in TiO2 (Anatase). 2. Voltammetry on Nanoporous Films. *J. Phys. Chem. B* **1997**, *101*, 7717−7722.

(69) Augustyn, V.; Come, J.; Lowe, M. A.; Kim, J. W.; Taberna, P.-L.; Tolbert, S. H.; Abruña, H. D.; Simon, P.; Dunn, B. High-Rate Electrochemical Energy Storage through Li+ Intercalation Pseudocapacitance. *Nat. Mater.* **2013**, *12*, 518−522.

(70) Xu, Y.; Zhang, C.; Zhou, M.; Fu, Q.; Zhao, C.; Wu, M.; Lei, Y. Highly Nitrogen Doped Carbon Nanofibers with Superior Rate Capability and Cyclability for Potassium Ion Batteries. *Nat. Commun.* **2018**, *9*, No. 1720.

(71) Wei, Q.; Xiong, F.; Tan, S.; Huang, L.; Lan, E. H.; Dunn, B.; Mai, L. Porous One-Dimensional Nanomaterials: Design, Fabrication and Applications in Electrochemical Energy Storage. *Adv. Mater.* **2017**, *29*, No. 1602300.